ELSEVIER

The assimilation of remotely sensed soil brightness temperature imagery into a land surface model using Ensemble Kalman filtering: a case study based on ESTAR measurements during SGP97

Wade T. Crow [*,1], Eric F. Wood

Environmental Engineering and Water Resources Program, Department of Civil and Environmental Engineering, Princeton University, Princeton, NJ 08544, USA

Abstract

An Ensemble Kalman filter (EnKF) is used to assimilate airborne measurements of 1.4 GHz surface brightness temperature (T_B) acquired during the 1997 Southern Great Plains Hydrology Experiment (SGP97) into the TOPMODEL-based Land–Atmosphere Transfer Scheme (TOPLATS). In this way, the potential of using EnKF-assimilated remote measurements of T_B to compensate land surface model predictions for errors arising from a climatological description of rainfall is assessed. The use of a real remotely sensed data source allows for a more complete examination of the challenges faced in implementing assimilation strategies than previous studies where observations were synthetically generated. Results demonstrate that the EnKF is an effective and computationally competitive strategy for the assimilation of remotely sensed T_B measurements into land surface models. The EnKF is capable of extracting spatial and temporal trends in root-zone (40 cm) soil water content from T_B measurements based solely on surface (5 cm) conditions. The accuracy of surface state and flux predictions made with the EnKF, ESTAR T_B measurements, and climatological rainfall data within the Central Facility site during SGP97 are shown to be superior to predictions derived from open loop modeling driven by sparse temporal sampling of rainfall at frequencies consistent with expectations of future missions designed to measure rainfall from space (6–10 observations per day). Specific assimilation challenges posed by inadequacies in land surface model physics and spatial support contrasts between model predictions and sensor retrievals are discussed.
© 2002 Elsevier Science Ltd. All rights reserved.

Keywords: Data assimilation; Land surface modeling; Microwave remote sensing; Soil moisture

1. Introduction

The steady accumulation of evidence suggesting that the accurate specification of root-zone soil moisture in numerical weather prediction models can improve seasonal weather prediction for certain locations on the globe (see e.g. [25]) has driven efforts to develop observational and modeling capabilities for soil moisture at continental-scales. Large-scale observational strategies have focused primarily on the potential of spaceborne microwave radiometry at low frequencies (<10 GHz) to infer surface (2–5 cm) soil water content. Results have been encouraging over lightly vegetated portions of the globe such as the Southern Great Plains (SGP) region in the south-central United States. The operational retrieval of soil moisture from space is expected to begin in earnest with the deployment of the 6.925 GHz Advanced Microwave Scanning Radiometer (AMSR-E) in 2002 and the 1.4 GHz Soil Moisture and Ocean Salinity (SMOS) sensor in 2005. Despite these advances, the utility of spaceborne soil moisture retrievals is hampered by several factors including: poor spatial resolution, limited vertical penetration depths, and low accuracy over heavily vegetated regions.

Recent modeling advances have centered on the Land Data Assimilation System (LDAS) project which demonstrates the feasibility of operationally modeling land surface water and energy balance processes at continental scales using forcing data obtained from both in situ and remote sensing sources. Soil moisture assimilation strategies constitute a logical extension of these

---

[*] Corresponding author.
E-mail address: wcrow@hydrolab.arsusda.gov (W.T. Crow).
[1] Present address: Hydrology and Remote Sensing Laboratory, ARS/USDA, Beltsville, MD 20705, USA.

advances by providing a strategy for efficiently combining soil moisture information derived from observational and modeling sources and, ideally, overcoming the limitations of each. For instance, assimilation of surface brightness temperature (T_B) measurements into physically based models of near surface heat and water transport can potentially increase both the effective vertical penetration [18] and horizontal resolution [34] of spaceborne radiometers. Conversely, sequential microwave brightness temperature measurements can aid land surface modelers in soil hydraulic parameter selection [3,27] and mitigating errors arising from poor model initialization [13].

Persisting concerns about its limitations, however, has led some to question the overall role of microwave soil moisture remote sensing in the study of land surface water and energy balance processes. An alternative strategy is to place additional emphasis on the remote observation of global land surface model forcings (e.g. precipitation, surface meteorology, and solar radiation) and develop 'open loop' modeling capabilities that operate without assimilated information. Comparisons between open loop and sequential soil moisture/T_B assimilation strategies have been made in a preliminary manner by [26]. However, a complete assessment requires actual remote measurements to realistically incorporate challenges arising from the interpretation of remotely sensed data and a viable assimilation strategy to combine model predictions and remote observations in a sound manner.

A variety of strategies for the assimilation of T_B measurements into land surface models have been introduced recently. The most effective strategies are based on either sequential assimilation using some variant of the Kalman filter (KF) algorithm [18,29] or non-sequential variational smoother approaches [20,35]. See [33] for a complete review of procedures. Of special interest here is the Ensemble Kalman filter (EnKF) introduced by [14] and applied to the problem of assimilating synthetically generated surface brightness temperature measurements into a land surface model by [36]. As noted by [36], the EnKF approach is attractive for the T_B assimilation problem because: (i) its sequential nature is well suited for assimilation of real-time observations into operational models, (ii) it is easy to implement for land surface models and does not require the calculation of an adjoint, (iii) the Monte Carlo nature of the ensemble generation allows for any statistical form or time/space correlation in error structure, and (iv) it does not require the computationally expensive dynamic updating of error/covariance information.

The purpose of this study is twofold. First, to extend the EnKF methodology described in [36] to a real-data case involving the assimilation of remotely sensed T_B data into a land surface model validated against independent observations. Second, to assess the ability of the EnKF to compensate predictions of surface latent heat flux and root-zone water storage for errors associated with the use of only climatological rainfall data. Such an assessment allows for comparison of the relative merits associated with land surface observations from a microwave radiometer versus precipitation estimates from a spaceborne radar.

2. The Ensemble Kalman filter

The EnKF is based on the generation of an ensemble of model predictions to estimate the error/covariance information required by the standard KF for the updating of model predictions with observations [14]. All error information is contained within the ensemble, avoiding the computationally expensive explicit propagation of the error covariance matrix.

The EnKF can be generalized using a state space representation of prediction and observation operators. The development and notation presented in this section follow the discussion presented in [36]. Take $\mathbf{Y}(t)$ to be a vector of land surface state variables at time t. The equation describing the evolution of these states, as determined by a potentially non-linear land surface model $\mathbf{f}$, is given by

$$\frac{d\mathbf{Y}}{dt} = \mathbf{f}(\mathbf{Y}, \mathbf{w}) \tag{1}$$

where $\mathbf{w}$ relates errors in model physics, parameterization, and/or forcing data and is taken to be mean zero with a covariance $\mathbf{C}_w$. The goal of the filtering problem is to constrain these predictions using a set of observations which are related to the model states contained in $\mathbf{Y}$. Let the operator $\mathbf{M}$ represent the observation process which relates $\mathbf{Y}$ to the actual measurements taken at time t_k

$$\mathbf{Z}_k = \mathbf{M}(\mathbf{Y}(t_k), \mathbf{v}_k) \tag{2}$$

where $\mathbf{v}_k$ represents Gaussian measurement error with covariance $\mathbf{C}_{vk}$. The EnKF is initialized by the introduction of synthetic Gaussian error into initial conditions and generating an ensemble of model predictions using Eq. (1). At the time of measurement, predictions made by the ith model replicate are referred to as the state forecast $\mathbf{Y}_-^i$. If $\mathbf{f}$ is linear and all errors are additive, independent and Gaussian, the optimal updating of $\mathbf{Y}_-^i$ by the measurement $\mathbf{Z}_k$ is given by

$$\mathbf{Y}_+^i = \mathbf{Y}_-^i + \mathbf{K}_k[\mathbf{Z}_k - \mathbf{M}_k(\mathbf{Y}_-^i)] \tag{3}$$

and

$$\mathbf{K}_k = [\mathbf{C}_{YM}(\mathbf{C}_M + \mathbf{C}_v)^{-1}]_{t=t_k} \tag{4}$$

where $\mathbf{C}_M$ is the error covariance matrix of the measurement forecasts $\mathbf{M}_k(\mathbf{Y}_-^i)$ and $\mathbf{C}_{YM}$ is the cross-covariance matrix linking the predicted measurements with the state variables contained in $\mathbf{Y}_-^i$. All covariance

values are statistically estimated around the ensemble mean. Here $\mathbf{Y}_+^i$ signifies the updated or analysis state representation. To ensure the Monte Carlo simulation converges to the same error predictions made by the standard KF, each assimilated measurement $\mathbf{Z}_k$ should be perturbed with synthetic measurement error consistent with the error characteristics contained in $\mathbf{C}_v$ [2].

Unlike the standard KF, the EnKF does not make use of a dynamic equation to explicitly update either $\mathbf{C}_M$ or $\mathbf{C}_{YM}$. Updating is based on a gain function $\mathbf{K}$ derived solely from information contained within the ensemble. Final state and measurement estimates are calculated by averaging predictions made by model replicates within the ensemble. While application of the EnKF does not explicitly require model linearity or Gaussian errors, the filter will cease to be optimal if either condition is not met.

3. Application during SGP97

Analysis was based on data collected during the 1997 Southern Great Plains Hydrology Experiment (SGP97) run within central Oklahoma between June 18 (Julian day 169) and July 18, 1997 (Julian day 199). During SGP97, L-band (1.4 GHz) surface brightness temperature observations were acquired with the electronically scanned thinned array radiometer (ESTAR) flown aboard a P3B aircraft. Usable 800-m T_B imagery was obtained on June 18, 19, 20, 25, 26, 27, 29, and 30, and on July 1, 2, 3, 11, 12, 13, 14, and 16. Ground-based soil moisture sampling was concentrated at three study areas within the transect imaged by ESTAR: the Central Facility area, the El Reno area, and the Little Washita Basin. See Fig. 1a for transect and study area locations and [23] for a complete description of SGP97 data collection and processing techniques.

Surface water and energy balance modeling was performed using the TOPMODEL-based Land–Atmosphere Transfer Scheme (TOPLATS) [15,31]. The Land Surface Microwave Emission Model (LSMEM) [12] was used to produce estimates of 1.4 GHz surface brightness temperature (T_B) based on TOPLATS surface state predictions. In this way, an ensemble of T_B predictions were calculated using a simple Poisson model of daily precipitation accumulations parameterized with climatological rainfall values. The surface state variables associated with each ensemble member were then updated by ESTAR T_B measurements using the EnKF framework reviewed in Section 2. The following subsections describe components of this methodology in greater detail.

3.1. TOPLATS modeling

The TOPLATS model version used was identical to that described by [31] except for the insertion of two additional computational layers in the model's soil water balance algorithm. Consequently, soil water balance calculations were made within four layers: 0–5, 5–15, 15–40, and 40 cm to the top of the water table. Diffusive and gravity drainage fluxes between layers were calculated using the numerical approximations presented in [31]. Following [40], evapotranspiration E was calculated as

$$E = \text{Min}\left[\sum_{i=1}^{4} \rho_i E_{\text{T}_i}, E_\text{p}\right] \qquad (5)$$

where E_{T_i} is the maximum rate of transpiration (i.e. the threshold transpiration) each soil layer i is capable of sustaining, ρ_i is the fraction of total root surface area in each soil layer, and E_p is the potential evapotranspiration. The relationship between soil moisture in layer i and E_{T_i} was taken from [17,39] and E_p was calculated assuming zero water stress and the Jarvis-type formulation presented in [31]. Soil temperature was calculated at surface (0 cm), 7.5, and 50 cm nodes.

Point-scale TOPLATS results were generated at the Department of Energy's Atmospheric Radiation Measurement Cloud and Radiation Testbed (ARM CART) extended facility (EF) site 13 (36°36′ N, 97°29′ W) near Lamont, Oklahoma and the National Oceanic and Atmospheric Administration/Atmospheric Turbulence and Diffusion Division (NOAA/ATDD) Little Washita Watershed site (34°58′ N, 97°57′ W) near Chickasha, Oklahoma. The ARM CART EF13 site is located within the Central Facility area and the NOAA/ATDD site in the northeastern corner of the Little Washita Basin. Land cover at both sites was classified as grassland/rangeland. Based on typical grassland conditions, the albedo of both sites was taken to be 0.20 [9] and the roughness length for momentum transfer to be 2.5 cm [1]. Forty percent (40%) of the root surface area was assigned to the 0–5-cm soil layer, 30% to the 5–15-cm layer, 20% to the 15–40-cm layer, and 10% to be below 40 cm. Parameters describing the threshold evapotranspiration of the grasses were taken from [6,16] and the impact of environmental factors on stomatal resistance followed the parameterization given in [31]. Plant heights at both sites were taken from [19].

Leaf area index (LAI) values for TOPLATS were tuned to improve latent heat flux (λE) predictions. The fitted LAI value for the Central Facility ARM CART EF13 site (LAI = 2.5) fell within the LAI measurement range for grass fields in the Central Facility area (LAI = 2.0 ± 0.6) [19]. However, the LAI value required at the Little Washita NOAA/ATDD site (LAI = 0.75) did not fall within the observed range for grass fields within the Little Washita Basin (LAI = 1.9 ± 0.2) and must therefore be considered a calibrated parameter. Following [22], soil texture was assumed to be loam at the ARM CART EF13 site and silt loam at
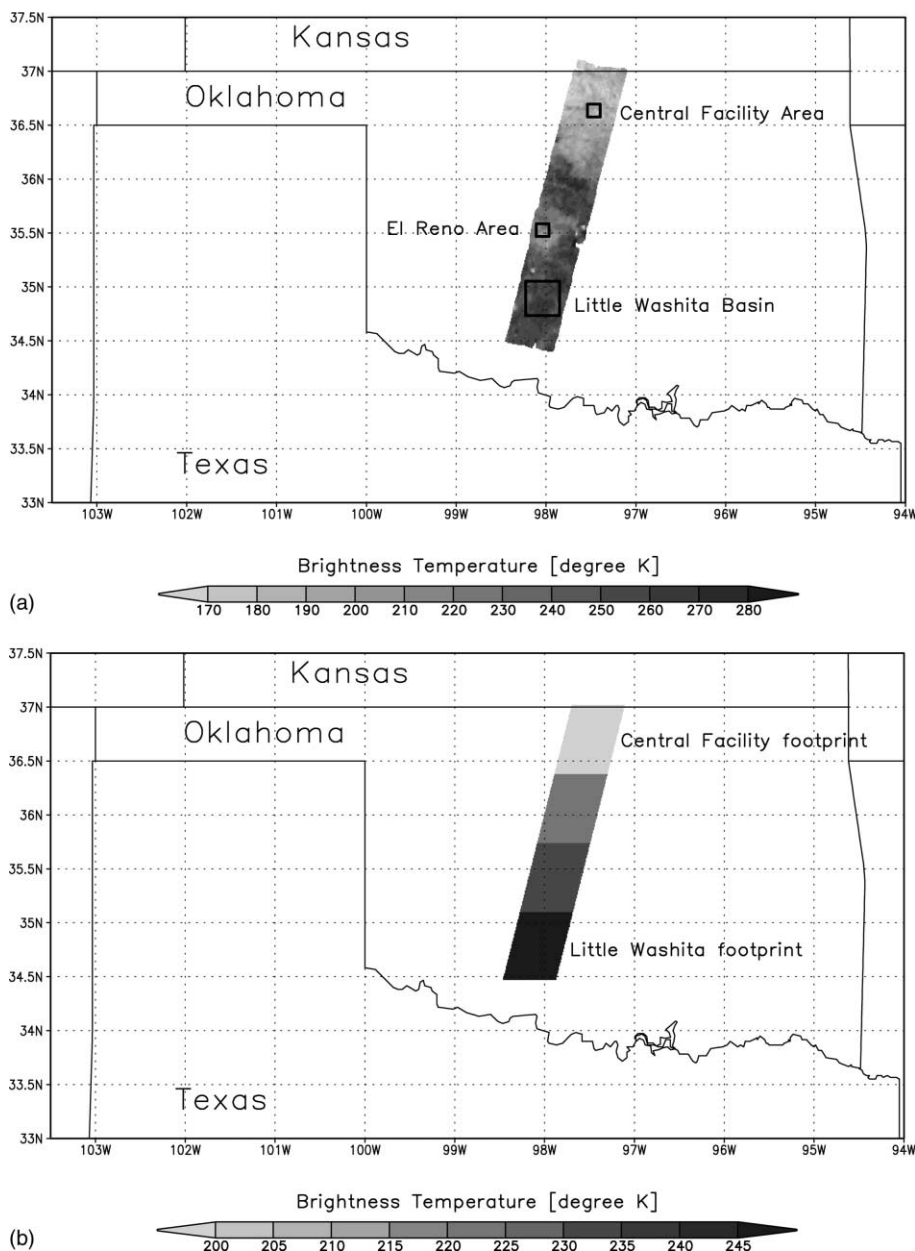
Fig. 1. (a) 800-m ESTAR brightness temperature image acquired on July 1, 1997 and study areas where intensive soil gravimetric sampling occurred. The ARM CART EF13 site is located within the Central Facility area and the NOAA/ATDD Little Washita Basin site in the northeastern corner of the Little Washita Basin. (b) Aggregation of the July 1 T_B imagery into four 50-km × 70-km footprint-scale pixels.

the NOAA/ATDD site. Soil hydraulic information was available from bore-hole data taken near all ARM CART sites. However, direct incorporation of in situ sampled values of soil parameters led to overly dry conditions at the ARM CART EF13 site. As a compromise, the in situ values at the ARM CART EF13 site were averaged with values suggested for loam soils by the lookup table presented in [32]. Since no bore-hold data was available at the NOAA/ATDD site, hydraulic parameters suggested by [32] for a silt loam soil were used directly. When available, surface soil moisture values were initialized with either gravimetric or soil

moisture probe measurements. Initial water table depths, deep soil moisture, and TOPLATS baseflow calibration parameters were set to climatologically reasonable values derived from long-term TOPLATS modeling of the region [7].

TOPLATS was also run on a 0.01° grid over the entire SGP97 ESTAR transect shown in Fig. 1 (15,810 computational pixels). At this larger scale, precipitation data was obtained from 4-km Weather Surveillance Radar (WSR-88D) hourly rainfall products, incoming solar radiation from 8-km Geostationary Operational Environmental Satellite (GOES) insolation imagery,

and other meteorological data from an interpolation of hourly National Climate Data Center (NCDC) station measurements. Land-cover data was obtained from a land-cover classification of the region performed by [11] and soil texture data from the multilayer soil characteristics data set (CONUS-SOIL) developed at Penn State University's Earth System Science Center [28]. Surface soil moisture was initialized using ESTAR-derived soil moisture created by [23] on June 18 (Julian day 169). As in the point-scale modeling, initial water table depths, deep soil moisture, and TOPLATS base-flow calibration parameters were set to climatologically reasonable values derived from long-term TOPLATS modeling of the region [7]. Soil hydraulic parameters were assigned using the look-up table presented in [32]. All vegetation present in pixels classified as winter wheat was assumed to be in senescence and not transpiring. Based on measurements presented in [19], 45% of winter wheat fields in the transect were assumed to be covered by senescent vegetation which effectively shaded the underlying soil and 55% were considered to be completely devoid of vegetative cover. The soil resistance scheme developed by [30] and incorporated into TOPLATS by [31] was used to model bare soil evaporation at these sites.

3.2. LSMEM modeling

Brightness temperature modeling by the LSMEM was based on surface (0–5 cm) soil moisture and a weighted combination of surface and 7.5-cm soil temperature predictions by TOPLATS. Various components of the LSMEM are based on previously published algorithms. Its calculation of soil dielectric is based on [10]. Reflectivity off a smooth surface is based on the two-layer model described in [38]. The impact of surface roughness is based on [4], and vegetation effects were incorporated using the model of [24]. Surface roughness, vegetation water content, and vegetation structure coefficients were taken from measurements made during SGP97 and processed by [23]. Vegetation coverage fraction was assumed to be 80% and the single scattering albedo off of the vegetation canopy to be 0.04 for all vegetation types. While both values are somewhat arbitrary, LSMEM T_B predictions during SGP97 exhibited little sensitivity to the specification of either parameter. Soil bulk density values were based on either ground sampling data (when available) or default values assigned according to the specified soil texture in the CONUS-SOIL classification. No atmospheric effects were incorporated into the microwave emission model.

3.3. TOPLATS/LSMEM validation

Point-scale TOPLATS state variable and flux predictions were validated using in situ flux tower data and gravimetric soil moisture measurements made during SGP97. In addition, TOPLATS/LSMEM T_B predictions were compared to ESTAR T_B observations over each site. Due to uncertainty concerning the georegistration of the ESTAR imagery [23], ESTAR observations were taken from the spatial average of retrievals within a 3×3 pixel window centered on each site. Validation results at the NOAA/ATDD Little Washita Basin and ARM CART EF13 sites are shown in Figs. 2 and 3 respectively. Comparisons to flux tower and gravimetric soil moisture observations are generally quite good, but discernible biases appear in model predictions of T_B and soil moisture relative to ESTAR observations. One source of this error is likely the difference between the spatial support of model predictions and the ESTAR observations. Conditions reflected by the model may be accurate within a local plot-scale (<100 m) but not representative of microwave emission for the entire 2.4^2-km^2 window (3×3 800-m pixels) from which ESTAR observations were obtained. For instance, ESTAR estimations of soil moisture over the entire 2.4^2-km^2 area containing the NOAA/ATDD site are biased low versus gravimetric samples taken immediately around the flux
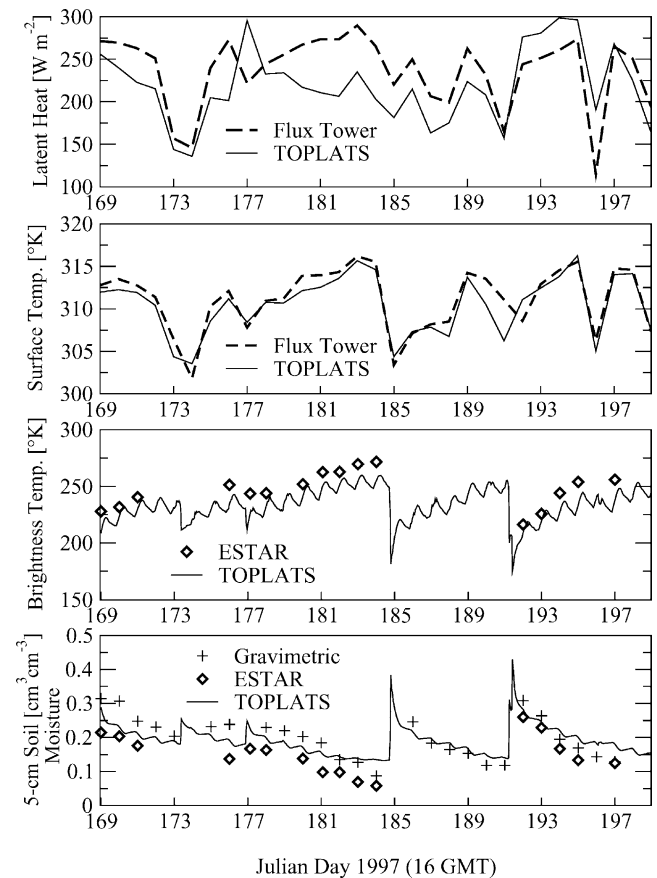

Fig. 2. Validation results for the NOAA/ATDD site within the Little Washita Basin. Latent heat flux and surface temperature values are daily averages of bowen ratio flux tower measurements made between 16 and 22 GMT (10 am and 5 pm CST).
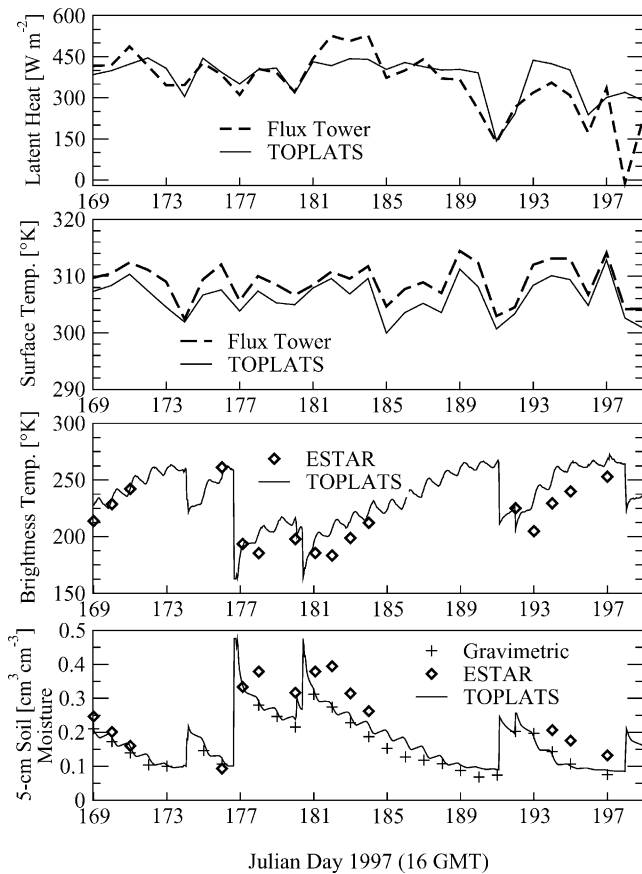
Fig. 3. Validation results for the ARM CART EF13 site within the Central Facility area. Latent heat flux and surface temperature values are daily averages of eddy correlation flux tower measurements made between 16 and 22 GMT (10 am and 5 pm CST).

tower site (Fig. 2). This suggests that the area surrounding the site is locally wet, and has a low T_B, relative to the larger 2.4^2-km^2 window in which the site is embedded. Because of georegistration uncertainty, comparisons did not improve when made between model predictions and the single 800^2-m^2 ESTAR pixel judged closest to each site.

Shortcomings in model physics can also lead to discrepancies between model results and observations. At the ARM CART EF13 site (Fig. 3) the model tends to overestimate T_B. Some of this overestimation occurs in the immediate aftermath of heavy rainfall events (see Julian days 178, 181, 182, and 193). Rainfall accumulations at the ARM CART EF13 site from June 18 to July 19 were at least double climatologically expected levels (>200 mm versus 90 mm). Consequently, one possible contributing factor to the overestimation of T_B is the presence of standing water in fields recently wetted by heavy rainfall. Standing water was observed, although not sampled gravimetrically, at the site during Julian days 181 and 182. The impact of this standing water, and the inability of the model to represent it, should introduce a high bias in modeled T_B predictions. In con-

trast to the ARM CART EF13 site, model estimates of T_B are biased low by 13.6 K at the NOAA/ATDD Little Washita Basin site (Fig. 2). Here comparisons to both ESTAR and gravimetric observations demonstrate that TOPLATS overestimates soil moisture during dry periods of the experiment (see Julian days 181–184 and 194–197 in Fig. 2). This overestimation is likely due to the neglect of bare soil evaporation beneath vegetation by TOPLATS and the accumulated drying power of this process during the tail end of dry-down events.

A more natural scale to compare model predictions and ESTAR T_B observations is at a spatial scale equivalent to the footprint size expected for next-generation spaceborne radiometers. Fig. 1b illustrates the division of the ESTAR transect into 4 approximately 50-km × 70-km footprints. Each footprint was modeled by TOPLATS/LSMEM using a 0.01° grid size. Scaling the analysis up to a footprint-scale overcomes some of the spatial support problems encountered at the site-scale. For instance, aggregating ESTAR observations and TOPLATS/LSMEM T_B predictions within the Little Washita footprint (see Fig. 1b) reduces the bias in TOPLATS/LSMEM T_B predictions from −13.6 K (observed at the NOAA/ATDD Little Washita Basin site) to −4.9 K.

A still coarser scale is obtained by averaging results for all four footprints in Fig. 1b into a single 50-km × 280-km transect-scale value. A comparison between transect-averaged T_B values obtained from ESTAR and TOPLATS/LSMEM modeling is shown in Fig. 4. At the transect-scale, LSMEM/TOPLATS T_B predictions remain biased slightly high. The bias is pronounced during dry periods of the simulation and likely reflects the continued overestimation of top 5-cm soil moisture by TOPLATS due to the neglect of bare soil evaporation below vegetation canopies. Despite this bias, independent surface soil moisture estimates derived from ESTAR and the model of [21] match TOPLATS/LSMEM predictions within a root-mean-squared (RMS) difference of 2.3% volumetric [0.023 cm$^3_{water}$ cm$^{-3}_{soil}$]. In addition, RMS differences between transect-averaged TOPLATS effective soil temperature estimates and those calculated by [23], using 10-cm Oklahoma Mesonet soil temperature measurements and the method of [5], are small (1.0 K).

3.4. Rainfall ensemble generation

The EnKF was applied to the problem of accurately modeling root-zone soil moisture using sequential observations of 1.4 GHz brightness T_B and no supporting rainfall data. Between each of the 16 ESTAR T_B acquisitions during SGP97, an ensemble of TOPLATS forecasts with 100 members was generated using climatological rainfall parameters and a daily rainfall model that assumed storms arrivals to be a Poisson process
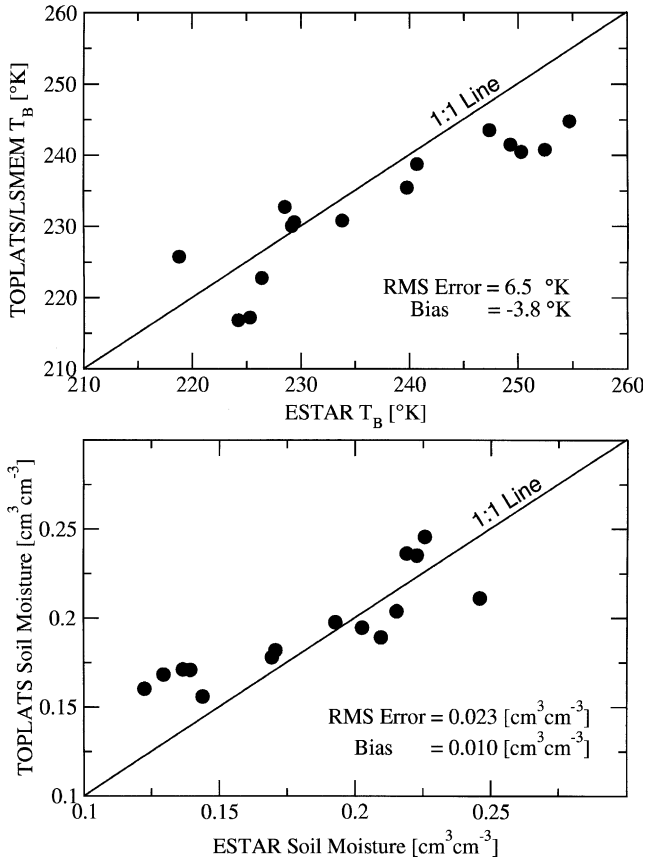
Fig. 4. Transect-averaged comparisons of ESTAR observations and TOPLATS/LSMEM predictions. ESTAR soil moisture values were taken from the data set generated by [23] using the radiative transfer model presented by [21].

Fig. 5. Updating of TOPLATS surface soil moisture and TOPLATS/LSMEM surface brightness temperature with local ESTAR T_B measurements and the EnKF at the ARM CART EF13 site. Shaded region represents 25th to 75th quartile spread of ensemble members. Dotted vertical lines indicate ESTAR observation times.

with exponentially distributed intensities. While simple in nature, such a model has been used successfully in previous soil moisture studies [37]. Daily rainfall depths were downscaled to hourly values by assuming all rainfall occurs within a continuous four-hour period randomly located within the day. Mean rainfall statistics during June and July for locations within the SGP97 study area were obtained from the Oklahoma State Climatology Service and rain gauge data collected between 1970 and 2001 at El Reno, Oklahoma (see Fig. 1a).

4. EnKF results

Fig. 5 illustrates the EnKF's sequential assimilation of ESTAR T_B measurements over the ARM CART EF13. The ensemble of TOPLATS/LSMEM predictions was initialized by adding mean zero Gaussian noise with a standard error of 3% volumetric to initial surface soil moisture values derived from ESTAR imagery on June 18 (Julian day 169). Between ESTAR overflights, an ensemble of TOPLATS runs, based on 100 separate
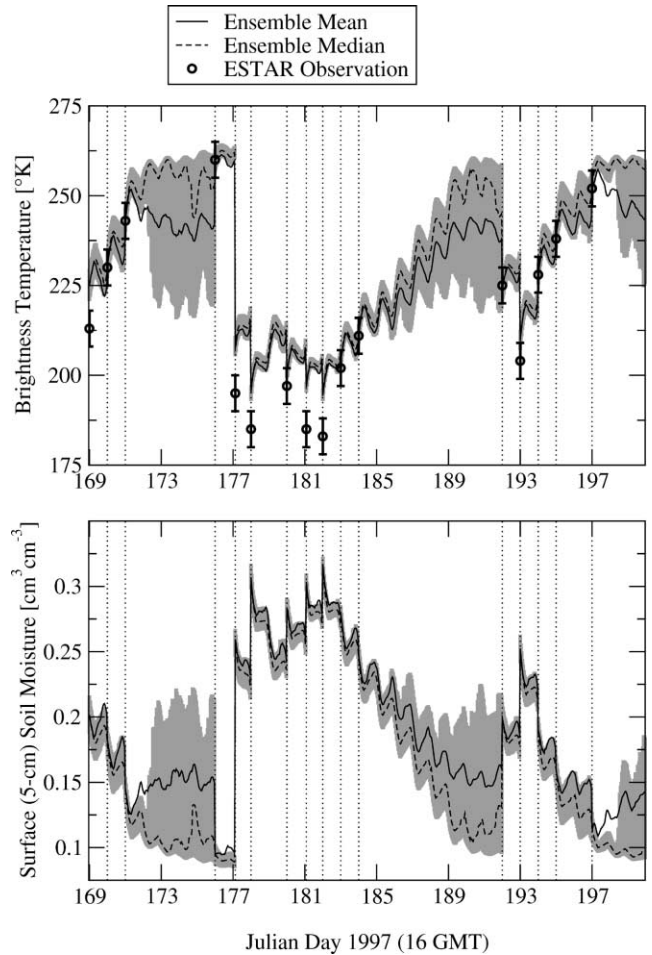
realizations of the Poisson/exponential rainfall model, was generated. At every observation time, model states for each of the ensemble members were updated using ESTAR T_B measurements and Eqs. (3) and (4). A standard error of 5 K was assumed for all ESTAR T_B measurements. The updated states constituted a new set of ensemble members which were then propagated to the next assimilation time by TOPLATS.

4.1. Point-scale results

Fig. 6 illustrates the ability of the EnKF and remotely sensed 1.4 GHz T_B measurements to correct errors in TOPLATS modeling results associated with the use of climatological rainfall information at the ARM CART EF13 site. EnKF results are shown for updating with both local- (2.4^2-km^2 resolution) and footprint-scale (50×70-km^2 resolution) ESTAR T_B observations. Benchmark TOPLATS results are based on modeling

Fig. 7. Baserun, EnKF, and open loop results for TOPLATS root-zone soil moisture predictions at the NOAA/ATDD Little Washita Basin site. EnKF results are shown for updating with both local- (2.4^2 km^2) and footprint-scale (50×70 km^2) T_B observations.
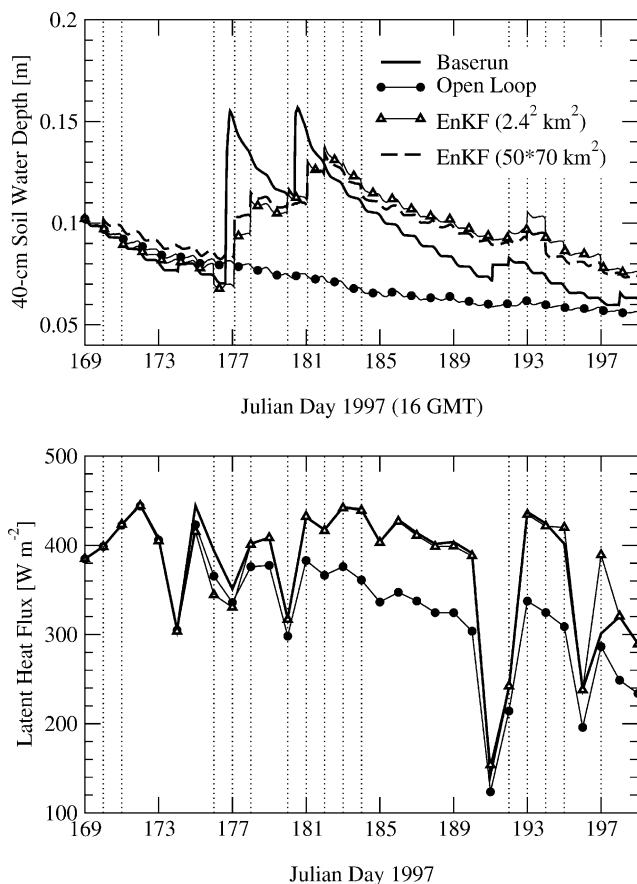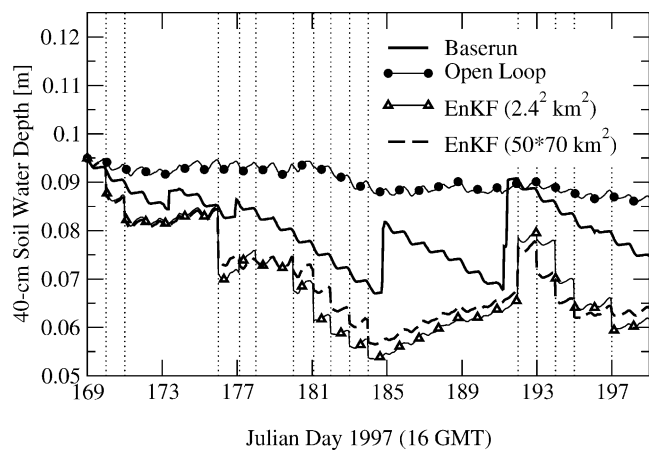

Fig. 6. Baserun, EnKF, and open loop results for TOPLATS predictions at the ARM CART EF13 site. EnKF results are shown for updating with local- (2.4^2 km^2) and footprint-scale (50×70 km^2) T_B observations. Latent heat flux values are daily averages between 16 and 22 GMT (10 am and 5 pm CST). Footprint-scale EnKF latent heat flux results are essentially identical to local-scale EnKF results and omitted from the plot for clarity.

with all available forcing data—including gauge-based rainfall measurements. Open loop results are derived from the average of 100 unupdated TOPLATS replicates generated with the climatologically based Poisson/exponential rainfall model. Since June and July 1997 were exceptionally wet at the site, assuming climatological rainfall levels generally underpredicts amounts of vertically integrated root-zone water storage ($\theta_{40\,cm}$) and surface latent heat flux (λE). Even without any direct rainfall measurements, updating members of the open loop ensemble with ESTAR T_B observations allows the EnKF to capture both the early dry portion of the experiment (Julian days 169 to 177) and the impact of rainfall events during the very wet middle period (Julian days 177 to 185). The improved representation of $\theta_{40\,cm}$ leads to more accurate λE predictions relative to the open loop case during the early and middle portion of the experiment. EnKF $\theta_{40\,cm}$ predictions, however, drift relative to benchmark results during the gap in ESTAR overflights between Julian days 184 and 192 and remain

biased high even after ESTAR measurements resume. The shortcomings of the EnKF during this period are attributable to a high bias in LSMEM T_B predictions during the final week of the experiment (see Fig. 2) which causes the filter to excessively wet the root-zone in an attempt to keep TOPLATS/LSMEM T_B predictions low enough to match ESTAR observations.

EnKF results from the NOAA/ATDD Little Washita Basin site shown in Fig. 7 are less encouraging. State predictions updated by the EnKF provide only marginally better results than the climatologically based open loop simulation. Some of the difficulty arises from a lack of ESTAR T_B observations between Julian days 184 and 192 which prevents an appropriate response to rainfall on day 185. However, EnKF $\theta_{40\,cm}$ results are consistently biased low even during an earlier period of near daily measurement rates between days 176 and 184. Despite relatively accurate TOPLATS predictions of surface soil moisture, a persistent low bias in benchmark LSMEM T_B predictions exists at the site (see Fig. 3). This bias in predicted T_B causes the EnKF to misinterpret ESTAR T_B observations and excessively dry the soil column. In particular, the poor EnKF update on day 176 is due to a combination of this bias and the large model uncertainty (i.e. ensemble spread in Fig. 5) arising from the ESTAR observation gap between days 171 and 176.

Somewhat surprisingly, EnKF results in Figs. 6 and 7 demonstrate little or no negative impact associated with upscaling ESTAR T_B observations from the local- to footprint-scale. This lack of dependence on resolution suggests that even coarse footprint-scale T_B retrievals have value for updating local point-scale models. However, the limited scope of the comparisons does not exclude other possibilities. For instance, the demonstrated value of the footprint-scale observations could

reflect the legacy of relatively large-scale precipitation patterns encountered during SGP97 or simply attest to the regional representativeness of the two study sites.

4.2. Impact of ensemble size

Even under ideal conditions for application of the EnKF (i.e. linear model, mean zero Gaussian observation and state errors) the EnKF will converge to an optimal result only when the size of the ensemble is sufficiently large. It is important to quantify the benefits of enhanced EnKF performance, realized with increased ensemble size, in the context of the additional computational costs. In a real-data case neither the true land surface state nor the exact measurement process connecting land surface state variables to remote observations is known. Consequently, evaluation of the benefits associated with increased ensemble size is difficult. Our best guess of land surface state conditions is given by TOPLATS/LSMEM results driven by gauge-measured precipitation and validated against observed surface state variable and flux measurements. These predictions are shown in Figs. 2 and 3 and used as the benchmark case in Figs. 4 and 5. Table 1 outlines RMS differences between such benchmark values and results derived from EnKF analysis with various ensemble sizes at the ARM CART EF13 site. Results are shown for four soil moisture and two surface temperature state variables and are based on the assimilation of local (2.4^2-km^2 resolution) ESTAR observations. While the EnKF clearly improves model predictions relative to the open loop case, little improvement is seen when increasing ensemble size between 50 and 1000. This suggests that, for ensemble sizes >50, alternative errors sources (e.g. measurement biases, lack of model linearity, non-Gaussian error distributions) and the shortcomings of the benchmark results themselves play a larger role than errors arising from finite ensemble sizes. In contrast, results in [36] demonstrate improved EnKF performance for ensemble sizes up to 1000. The larger range of dependence in [36] is likely due to the much higher number of degrees of freedom implicit in their horizontally distributed update procedure relative to the one-dimensional case examined here.

4.3. Comparison to spaceborne radar rainfall and direct insertion results

A natural benchmark for EnKF results are TOPLATS predictions based on rainfall times series derived from temporal sampling patterns consistent with expectations for next-generation spaceborne missions designed to measure precipitation globally. Sparse (6–10 samples per day) sampling of precipitation by spaceborne radar is generally considered to be a major source of error in satellite-derived estimates of rainfall accumulations (see e.g. [41]). Assuming rainfall rates to be temporally constant between sparse measurements can lead to large errors in estimations of hourly rainfall rates and impact the accuracy of land surface model predictions driven by spaceborne precipitation observations.

Fig. 8 addresses this concern by comparing the RMS accuracy of $\theta_{40\,cm}$ and λE TOPLATS predictions derived from a range of sparse sampling rates to errors associated with the assimilation of local (2.4^2-km^2 resolution) T_B observations and purely climatological rainfall considerations. Comparisons were made using a subsampling procedure on 15-min rainfall gauge data at the ARM CART EF13 site. For a daily sampling frequency of v, rainfall rates were assumed content and equal to the observed 15-min gauge-derived rate for the $24v^{-1}$ h period centered on each observation. The subsampling exercise was repeated using every 15-min observation in the first $24v^{-1}$ interval as the simulation start time. The resulting set of rainfall forcing data was then used to force an analogous set of TOPLATS observations from which error statistics in Fig. 8 were calculated.

Since the actual integration time of each rain gauge measurement is 15 min, and not the nearly instantaneous snapshot provided by a satellite, rainfall sampling errors in Fig. 8 are likely conservative. Nevertheless, for sampling rates expected in next-generation global precipitation missions (6–10 observations per day), EnKF $\theta_{40\,cm}$ and λE results driven by climatological rainfall information and assimilated 1.4 GHz T_B values are more accurate than results derived from open loop strategies based on the sparse temporal sampling of precipitation from space.

Table 1
Errors in EnKF soil moisture (θ) and temperature (T) predictions for various ensemble sizes at the ARM CART EF13 site

Ensemble size	$\theta_{5\,cm}$	$\theta_{5-15\,cm}$	$\theta_{15-40\,cm}$	θ_{tz}	T_{surf}	$T_{7.5\,cm}$
50	0.87	0.81	0.59	0.46	0.45	0.92
100	0.88	0.81	0.53	0.36	0.50	0.93
200	0.87	0.81	0.53	0.31	0.52	0.91
500	0.85	0.80	0.52	0.35	0.49	0.89
1000	0.85	0.80	0.54	0.41	0.52	0.92

The transmission zone (θ_{tz}) extends from a depth of 40 cm to the top of the water table. T_{surf} is the surface skin temperature and $T_{7.5\,cm}$ is the 7.5-cm soil temperature. All error values are calculated relative to a TOPLATS baserun simulation forced by gauge-based rainfall observations and normalized by the error observed in the open loop case.
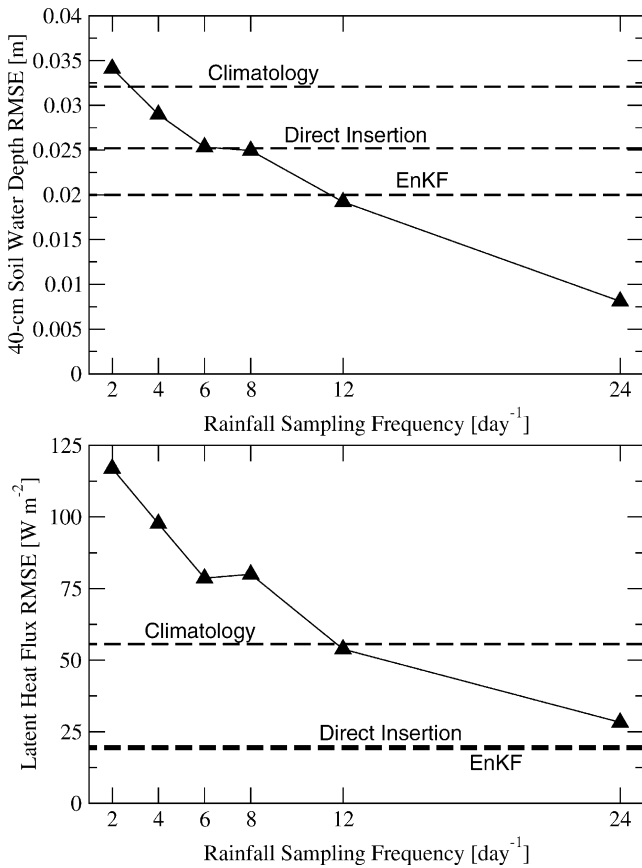
Fig. 8. Errors at the ARM CART EF13 site associated with the EnKF (local ESTAR T_B observations), the climatologically driven open loop, and direct insertion strategies (local ESTAR surface soil moisture retrievals) plotted with errors due to the sparse temporal sampling of rainfall. Latent heat flux RMS error is given in terms of daily averages between 16 and 22 GMT (10 am and 5 pm CST).

Results for the direct insertion of soil moisture values derived from ESTAR T_B imagery and the backwards radiative transfer model of [21] are also shown in Fig. 8 for comparison. As in the EnKF case, results for direct insertion were obtained by running an ensemble of climatologically derived rainfall realizations through TOPLATS/LSMEM. At each observation time, surface (5-cm) soil moisture in each realization was set equal to the local ESTAR soil moisture observation. All other model state variables were unchanged, and final state variable predictions were obtained by averaging across the ensemble.

Such an integration strategy is generally considered suboptimal because it neglects information generated by the model and updates only the single state variable—surface soil moisture—directly observed by ESTAR. Large rainfall events on Julian days 177 and 181 at the ARM CART 13 site, for instance, recharge soil moisture levels far below the 5-cm surface zone. Direct insertion updating is incapable of capturing such recharge and underpredicts subsequent levels of root-zone water storage at the site. Fig. 8 demonstrates the relative su-

periority of EnKF-derived root-zone soil moisture over direct insertion results during SGP97. Due to wet conditions at the site, which minimize the sensitivity of surface energy fluxes to soil water availability, the EnKF's advantage over direct insertion is very slight for λE predictions (Fig. 8).

4.4. Footprint-scale results

For footprint-scale simulations, 800-m ESTAR T_B imagery was aggregated up to the four footprint-scales shown in Fig. 1b. TOPLATS/LSMEM predictions for every one of the ~4000 computational grid-cells within each footprint were updated using these spatially averaged ESTAR T_B measurements and the EnKF framework. For computational reasons, the ensemble size (i.e. number of model replicates) was reduced from 100 to 50. Ensemble replicates were generated using the same daily rainfall model as the site-scale analysis. Rainfall
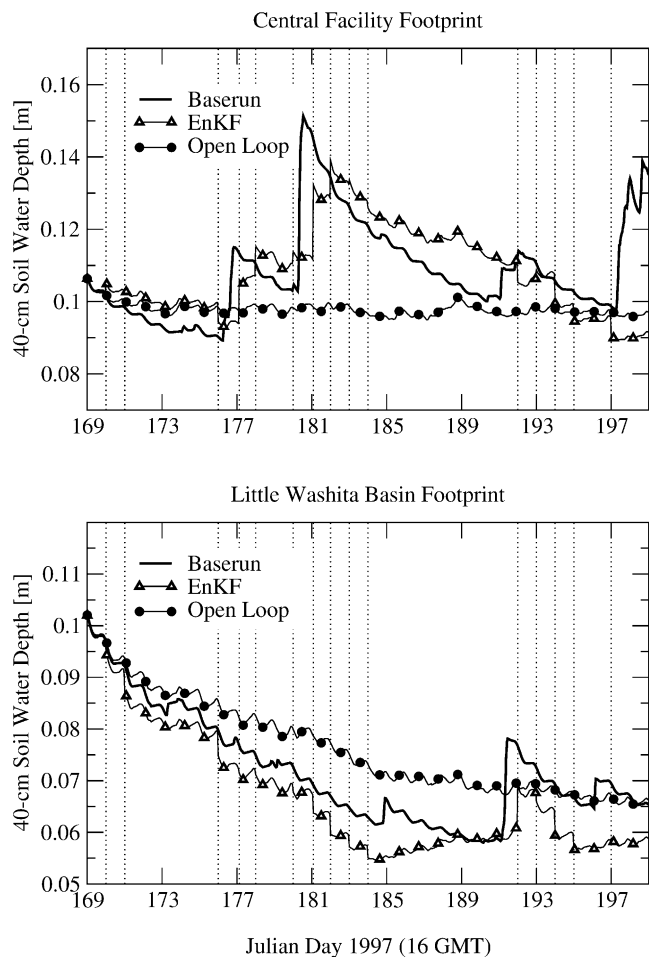

Fig. 9. Baserun, EnKF assimilation, and open loop root-zone soil moisture predictions over the Central Facility and Little Washita footprints (see Fig. 1b). Baserun results are generated by TOPLATS with full WSR-88D rainfall information. Dotted vertical lines indicate ESTAR observation times.

realizations were independently generated for each of the four footprint-scale pixels and rainfall intensities were assumed to be homogeneous within each footprint.

A north–south gradient in rainfall accumulations developed during SGP97. Rainfall levels in the northernmost footprint-scale pixel (the Central Facility footprint) were several times larger than the climatological mean, while accumulations in the southernmost pixel (the Little Washita footprint) were below normal. Fig. 9 illustrates the ability of the EnKF, driven solely by T_B observations derived from the top 5 cm of the soil column and climatological rainfall considerations, to resolve these deviations from expected rainfall levels. During the first half of the experiment, the EnKF is able to effectively reproduce the impact of spatial rainfall anomalies by adding soil water to the root-zone within the Central Facility footprint and removing water within the Little Washita footprint. Capturing this spatial soil water pattern allows for the improved pre-
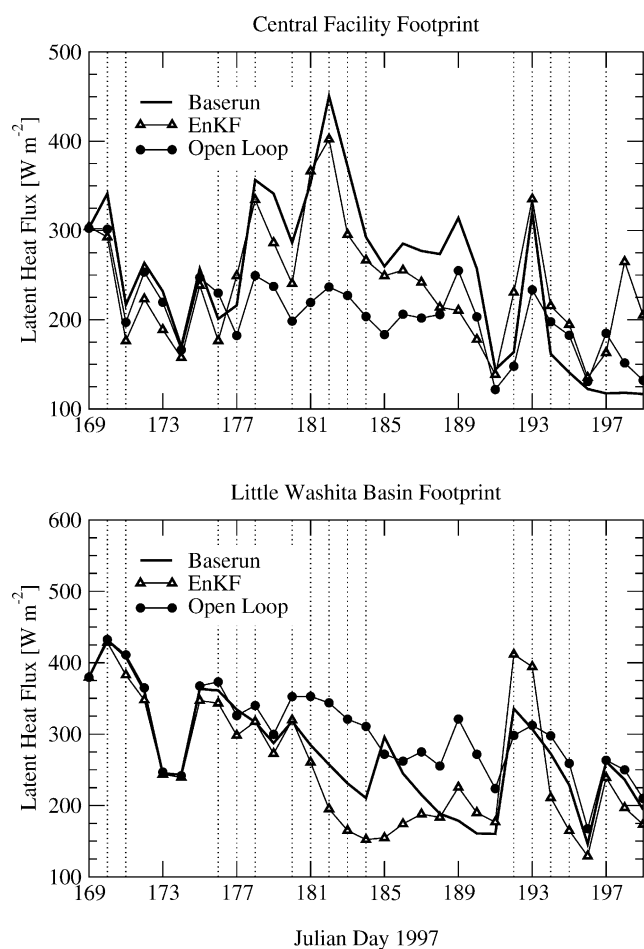

Fig. 10. Baserun, EnKF assimilation, and open loop latent heat flux predictions over the Central Facility and Little Washita footprints (Fig. 1b). Baserun results are generated by TOPLATS with full WSR-88D rainfall information. Dotted vertical lines indicate ESTAR observation times. Plotted values are daily averages between 16 and 22 GMT (10 am and 5 pm CST).

diction of surface latent heat flux within both footprints (Fig. 10). However, as in the point-scale case, EnKF predictions are less accurate following the temporal gap in observations between Julian days 184 and 192. During the final week of SGP97, the EnKF does not outperform the open loop simulations for either footprint-scale pixel (see Figs. 9 and 10). Additional study is required to determine if this is a direct consequence of the eight-day observation gap or if it represents a more general drift in EnKF-derived state predictions. Rainfall levels in the two footprint-scale pixels between the Central Facility and Little Washita footprints (see Fig. 1b) were near climatological expectations. Consequently, assimilating T_B adds little to surface state and flux predictions made with the open loop simulations.

5. Discussion and conclusions

Results illustrate both the challenges and potential benefits of using the EnKF strategy presented by [36] to assimilate actual remote observations of surface brightness temperature into a surface water and energy balance model. Clearly, the assimilation process presented in the Section 3 does not meet all the requirements for the EnKF to be an optimal filter. For instance, the method used to generate TOPLATS replicates tends to produce skewed model ensembles and a non-Gaussian error structure (Fig. 5). In fact, several time steps in Fig. 5 demonstrate sufficient skew such that the ensemble mean falls outside of the inner two quartiles of the distribution. Such non-Gaussian error structure almost certainly has a negative impact on the EnKF's performance. In addition, not all sources of model and measurement error are implemented within the ensemble generation procedure. Even if rainfall and T_B were measured perfectly, model errors would still lead to differences between predicted and observed T_B. Some of this error is attributable to model physics like the neglect of bare soil evaporation beneath vegetation in TOPLATS and the inability of the LSMEM to capture the impact of standing water on land surface microwave emission. However, even in cases where model predictions are relatively accurate, temporally persistent biases can arise from contrasts between the spatial support of model predictions and measurement footprints [8]. This appears to be the case for point-scale results at the NOAA/ATDD Little Washita Basin site where the misinterpretation of T_B observations by the filter, combined with gaps in the time series of ESTAR T_B observations, leads to the excessive removal of water from the soil column (Fig. 7).

Ideally, all such error sources should be accounted for in an assimilation strategy. However, while some description of model error and measurement bias may be obtainable from either ground-based validation efforts

or statistical analysis of filter innovations, it is unlikely that a full description of model error will be available in operational settings at large scales. As a result, no attempt was made to correct EnKF predictions for the impact of model error other than that arising from a lack of rainfall data. This was done under the assumption that difficulties with spatial support, inaccurate model physics, and measurement bias are an unavoidable part of attempting to compare and combine model predictions with remotely sensed observations and should be reflected in any realistic assessment of assimilation strategy merit.

Despite these challenges, results at the ARM CART EF13 site and over coarser footprint-scales are encouraging. Root-zone soil moisture predictions made with the EnKF, T_B observations approximately once every other day, and climatological rainfall expectations at the ARM CART EF13 site are more accurate than predictions derived from either direct assimilation of ESTAR surface soil moisture imagery or predictions based on sampling rainfall rates with temporal frequencies comparable to expectations for future spaceborne radar precipitation missions (Fig. 8). Even when hampered by no direct rainfall information and constraints expected in next-generation spaceborne remote sensors (i.e. 5-cm measurement depth and 50-km × 70-km horizontal resolution), EnKF-assimilated ESTAR measurements are capable of representing the impact of spatially heterogeneous rainfall on root-zone (40 cm) soil moisture along the SGP97 transect (Fig. 9). Finally, these results are obtainable with relatively small ensemble sizes (50–100)—suggesting that the EnKF strategy is computationally competitive with other assimilation approaches.

The representation of rainfall and rainfall uncertainty utilized here is clearly simplistic and not meant to represent current observational capabilities within the SGP region. Rather, the purpose is to evaluate the potential of the EnKF and remote measurements of 1.4 GHz T_B to compensate land surface model predictions for errors associated with a simplistic or inaccurate representation of rainfall. More realistic assimilation approaches should take full advantage of capabilities for observing and predicting precipitation at global scales. For instance, of more use than a simple comparison of the relative advantage associated with measuring either 1.4 GHz T_B or rainfall at sparse sampling frequencies, is a strategy for integrating both types of measurements in the context of an assimilation strategy. One potential area for future study is using an EnKF framework to facilitate this integration. However temporally sparse, measurements from a spaceborne precipitation mission contain information that can be used to condition the rainfall forecast ensemble, derived here from purely climatological considerations, and improve the assimilation of surface T_B measurements. Similar conditioning is possible using sparse spatial data from rainfall gauge

networks or quantitative precipitation forecasts derived from regional weather prediction models. Finally, given that the operational measurement of 1.4 GHz T_B from space is not expected before 2006, an important extension of this work is the application of the EnKF to C-band (6.925 GHz) AMSR-E T_B observations expected in the near-future. The enhanced impact of vegetation and atmospheric effects at higher C-band frequencies poses an additional challenge for assimilation approaches.

Acknowledgements

References

[1] Brutsaert W. Evaporation into the atmosphere. Dordrecht, Holland; 1982. 299pp.

[2] Burgers G, van Leeuwen PJ, Evensen G. Analysis scheme in the Ensemble Kalman filter. Mon Weather Rev 1998;126:1719–24.

[3] Burke EJ, Gurney RJ, Simmonds LP, Jackson TJ. Calibrating a soil water and energy balance model with remotely sensed data to obtain qualitative information about the soil. Water Resour Res 1997;33:1689–97.

[4] Choudhury BJ, Schmugge TJ, Chang A, Newton RW. Effect of surface roughness on the microwave emission from soils. J Geophys Res 1979;84:5699–706.

[5] Choudhury BJ, Schmugge TJ, Mo T. A parameterization of effective temperature for microwave emission. J Geophys Res 1982;87:1301–4.

[6] Choudhury BJ, Idso SB. Evaluating plant and canopy resistances of field grown wheat from concurrent diurnal observations of leaf water potential, stomatal resistance, canopy temperature, and evapotranspiration flux. Agric Forest Meteor 1985;34:67–76.

[7] Crow WT. The impact of land surface heterogeneity on the accuracy and utility of spaceborne soil moisture retrievals. PhD dissertation, Dept Civil Environ Eng, Princeton University, Princeton, NJ, 2001.

[8] Crow WT, Drusch M, Wood EF. An observation system simulation experiment for the impact of land surface heterogeneity on AMSR-E soil moisture retrieval. IEEE Trans Geosci Remote Sens 2001;39:1622–31.

[9] Dingman SL. Physical hydrology. Englewood Cliffs, NJ: Prentice-Hall; 1994, 575pp.

[10] Dobson MC, Ulaby FT, Hallikainen MT, El-Reyes MA. Microwave dielectric behavior of wet soil—part II: dielectric mixing models. IEEE Trans Geosci Remote Sens 1985;23:35–46.

[11] Doriaswamy P, Stern AJ, Cook PW. Classification techniques for mapping biophysical parameters in the US Southern Great Plains. In: Proc Int Geoscience Remote Sensing Symp, IEEE Cat no. 007803-4403, 1998. p. 862–5.

[12] Drusch M, Wood EF, Jackson TJ. Vegetative and atmospheric corrections for soil moisture retrieval from passive microwave remote sensing data. J Hydrometeor 2001;24:256–64.

[13] Entekhabi D, Nakamura H, Njoku EG. Solving the inverse problem for soil moisture and temperature profiles by sequential assimilation of multifrequency remotely sensed observations. IEEE Trans Geosci Remote Sens 1994;32:438–47.

[14] Evensen G. Sequential data assimilation with a nonlinear quasi-geostrophic model using Monte Carlo methods to forecast error statistics. J Geophys Res 1994;99:10143–62.

[15] Famiglietti JF, Wood EF. Multiscale modeling of spatially variable water and energy balance processes. Water Resour Res 1994;30:3061–78.

[16] Feddes RA, Rijetma PE. Water withdrawal by plant roots. J Hydrol 1972;17:33–59.

[17] Feyen J, Belmans C, Hillel D. Comparison between measured and simulated plant water potential during soil water extraction by potted ryegrass. Soil Sci 1980;129:180–5.

[18] Galantowicz JF, Entekhabi D, Njoku EG. Tests of sequential data assimilation for retrieving profile soil moisture and temperature from observed L-band radiobrightness. IEEE Trans Geosci Remote Sens 1999;37:1860–70.

[19] Hollinger SE, Daughtry CST. Southern Great Plains 1997 Hydrology Experiment: Vegetation sampling and data documentation. Report to United States Department of Agriculture on Contract AG-58-1270-7-043, 1999.

[20] Houser PJ, Schuttleworth WJ, Famiglietti JS, Gupta HV, Syed KH, Goodrich DC. Integration of soil moisture remote sensing and hydrologic modeling using data assimilation. Water Resour Res 1998;34:3405–20.

[21] Jackson TJ, Le Vine DM, Swift CT, Schmugge TJ, Schiebe FR. Large area mapping of soil moisture using the ESTAR passive microwave radiometer in Washita'92. Remote Sens Environ 1995;53:27–37.

[22] Jackson TJ. Southern Great Plains 1997 (SGP97) Hydrology Experiment Plan. Available from: http://hydrolab.arsusda.gov/sgp97.

[23] Jackson TJ, LeVine DM, Hsu AY, Oldak A, Starks PJ, Swift CT, et al. Soil moisture mapping at regional scales using microwave radiometry: the Southern Great Plains Hydrology Experiment. IEEE Trans Geosci Remote Sens 1999;37:2136–50.

[24] Kirdiashev KP, Chukhlantsev AA, Shutko AM. Microwave radiation of the earth's surface in the presence of vegetation. Radio Eng Electron 1979;24:256–64.

[25] Koster RD, Suarez MJ, Heiser M. Variance and predictability of precipitation at seasonal to interannual time scales. J Hydrometeor 2000;1:26–46.

[26] Li J, Islam S. Estimation of soil moisture profile and surface fluxes partitioning from sequential assimilation of surface layer soil moisture. J Hydrol 1999;220:86–103.

[27] Mattikalli NM, Engman ET, Jackson TJ, Ahuja LR. Microwave remote sensing of temporal variations of brightness temperature and near-surface soil water content during a watershed-scale field experiment, and its application to the estimation of soil physical properties. Water Resour Res 1998;34:2289–99.

[28] Miller DA, White RA. A conterminous United States multilayer soil characteristics data set of regional climate and hydrology. Earth Interact 1998;2:1–15.

[29] Milly PCD, Kabala J. Integrated modeling and remote sensing of soil moisture. In: Hydrologic Applications of Space Technology (Proc Cocoa Beach Workshop, FL, August 1985), IAHS Publ. 160, 1986. p. 331–9.

[30] Passerat de Silans A. Transferts de masse et de chaleur dan on sol strateifi'e soumis 'a une excitation atmosph'erique naturelle. Comparison: Mod'eles-exp'erience. PhD dissertation, Int. Nat. Polytech. de Grenoble, Grenoble, France, 1986.

[31] Peters-Lidard CD, Zion MS, Wood EF. A soil-vegetation-atmosphere transfer scheme for modeling spatially variable water and energy balance processes. J Geophys Res 1997;102:4303–24.

[32] Rawls WJ, Brakensiek DL, Saxton KE. Estimation of soil properties. Trans ASAE 1982;25:1316–20.

[33] Reichle RH. Variational data assimilation of microwave radio-brightness observations for land surface hydrology applications. PhD dissertation, Dept Civil Environ Eng, Mass Inst Technol, Cambridge, MA, 2000.

[34] Reichle RH, Entekhabi D, McLaughlin DB. Downscaling of radiobrightness temperature measurements for soil moisture estimation: a four-dimensional variational data assimilation approach. Water Resour Res 2001;31:2353–64.

[35] Reichle RH, McLaughlin DB, Entekhabi D. Variational data assimilation of microwave radiobrightness observations for land surface hydrology applications. IEEE Trans Geosci Remote Sens 2001;39:1708–19.

[36] Reichle RH, McLaughlin DB, Entekhabi D. Hydrologic data assimilation with the Ensemble Kalman filter. Mon Weather Rev 2002;130:103–14.

[37] Salvucci GD. Estimating the moisture dependence of root-zone water loss using conditionally averaged precipitation. Water Resour Res 2001;37:1357–65.

[38] Ulaby FW, Moore K, Fung AK. Microwave remote sensing: active and passive, vol. III. Norwell, MA, Artech House; 1982.

[39] Wetzel P, Chang J. Concerning the relationship between evapotranspiration and soil moisture. J Clim Appl Meteor 1987;26:18–27.

[40] Wetzel P, Chang J. Evapotranspiration from nonuniform surfaces: a first approach for short-term numerical weather predictions. Mon Weather Rev 1988;116:600–21.

[41] Wilheit TT. Error analysis for the Tropical Rainfall Measuring Mission (TRMM). In: Theon JS, Fugano N, editors. Tropical rainfall measurements. A. Deepak, Hampton, Va., 1988. p. 377–85.